IEEE Access
Multidisciplinary ⋮ Rapid Review ⋮ Open Access Journal

Received 28 May 2024, accepted 10 July 2024, date of publication 15 July 2024, date of current version 24 July 2024.

*Digital Object Identifier 10.1109/ACCESS.2024.3427860*

RESEARCH ARTICLE

# Joint Design of Autocorrelation and Spectral Characteristics of Radar Waveforms

**OMAR ALDAYEL, (Member, IEEE), ESAM M. ALMOHIMMAH, AMR M. RAGHEB, AHMED ALMAIMAN, AND SALEH A. ALSHEBEILI**
Electrical Engineering Department, King Saud University, Riyadh 11421, Saudi Arabia
Corresponding author: Esam M. Almohimmah (ealmohimmah@ksu.edu.sa)

This work was supported by the Researchers Supporting Project, King Saud University, Riyadh, Saudi Arabia, under Grant RSP2024R46.

**ABSTRACT** One important aspect of radar systems is the transmit waveform, which plays a key role in defining system's detection capability and target resolution. Waveforms with good autocorrelations and increased bandwidth are preferred for this purpose. However, waveforms with large bandwidths may cause spectral interference with neighboring channels. As a result, it is crucial to establish frequency stopbands within the spectrum of transmit waveform to mitigate potential interference. While it's easy to independently design waveforms with either good autocorrelation or specific frequency stopbands, designing radar waveforms that excel in both aspects simultaneously is a difficult task. In this paper, we address this challenge by optimizing radar waveform with dual objectives: minimizing autocorrelation sidelobes to enhance system performance and managing spectral characteristics to expand bandwidth while avoiding interference with other frequency bands. We first transform the dual-objective function into a single-objective function encompassing both correlation and stopband properties. We propose a novel algorithm to solve this problem and rigorously demonstrate its convergence through mathematical proof, providing a robust foundation for practical implementation. We evaluate the algorithm's performance in challenging scenarios and demonstrate its effectiveness compared to recent approaches in the literature.

**INDEX TERMS** Waveform design, dual-objective optimization, autocorrelation sidelobes, spectral shaping, stopbands, frequency nulling.

## I. INTRODUCTION

Waveform design plays a crucial role in various fields, including radar and communication systems. The fundamental objective in waveform design is to create waveforms with favorable properties while adhering to specific constraints [1]. For instance, waveform design can be employed to generate waveforms with a high-quality autocorrelation function (ACF) [2], [3], [4], minimize cross-correlation [5], [6], shape the ambiguity function of the waveform [7], [8], synthesize beampatterns [9], [10], optimize frequency diverse arrays (FDAs) [11], [12], and control spectral characteristics [13], [14]. Recently, there has been a focus on generating radar waveforms with two objectives. The first objective is minimizing the ACF's sidelobes to improve system performance. This objective can be met by minimizing the integrated sidelobe level (ISL) or minimizing the peak sidelobe level (PSL) [15]. The second objective is managing spectral characteristics to expand waveform bandwidth while preventing interference with other occupied bands. This objective can be achieved by suppressing or minimizing waveform energy in interfering frequency bands [13]. Solving this dual-objective optimization problem is highly challenging due to the intricate trade-off between the necessity for impulse-like autocorrelation, leading to a flat spectrum, and the requirement for a radar waveform with one or more stopbands.

### A. RELATED WORK

There are many studies in the literature that tackle this dual-objective optimization problem. In [16], the classical stopband cyclic algorithm new (SCAN) and weighted SCAN (WeSCAN) were proposed for designing unimodular sequences with desirable characteristics in terms of low spectral power within specific frequency bands and low correlation sidelobes. The SCAN algorithm utilizes fast Fourier transform (FFT) operations, enabling efficient handling of extended sequence designs. On the other hand, the WeSCAN

The associate editor coordinating the review of this manuscript and approving it for publication was Nagendra Prasad Pathak.

algorithm offers greater flexibility in controlling the trade-off between frequency stopband and correlation sidelobe suppression. In [17], the challenge of waveform design, under the constraints of spectral shape and unit modulus, was formulated as a nonlinear constrained optimization problem. To address this challenge, the study utilized auxiliary variable neurons and Lagrange neurons within the framework of the Lagrange programming neural network. In [18], an FFT-based conjugate gradient algorithm (FCGA) for designing periodic or aperiodic waveforms with low autocorrelation and frequency stopband properties was proposed. The connection between the power spectrum density and the autocorrelation function was leveraged to formulate the problem as an unconstrained minimization problem of the sequence phases. Moreover, Taylor series expansion was utilized to deduce the search step size of the FCGA. In [19], a method for generating unimodular sequences that exhibit a low PSL and adjustable stopband attenuation was proposed. The optimization problem was transformed into a convex one using alternating minimization and exact penalty approach (AM-EPA) techniques. Subsequently, this convex problem was solved using CVX, a package for specifying and solving convex programs [20]. Furthermore, a theoretical lower bound for the PSL minimization problem is established, considering spectral and unimodular constraints. In [21], a fast and efficient algorithm was introduced to design unimodular waveforms with low autocorrelation sidelobes and desired spectral stopbands. The proposed algorithm is based on the Limited Memory Broyden-Fletcher-Goldfarb-Shanno (L-BFGS) optimization method, which is termed L-BFGS-based Sequence Design (LBSD).

While numerous waveform design algorithms have been proposed in the literature to address this dual optimization challenge, most of them struggle to deliver satisfactory results due to the inherent trade-off between the two objectives. For instance, prioritizing the ACF of the generated waveform often results in relatively high residual energy in the stopbands, potentially causing interference with other channels operating within these frequency bands. Conversely, emphasizing the level of the stopbands in the generated waveform results in a low-quality ACF with high sidelobe levels. Furthermore, most of the existing waveform design studies do not provide mathematical proof of convergence.

### B. CONTRIBUTION

In this paper, we address the challenge of the dual-objective optimization of radar waveforms for jointly minimizing the autocorrelation sidelobes and the spectral stopbands level. The contribution of this paper is summarized as follows

1) **Algorithm Development**: We develop a novel waveform design algorithm, named Joint Minimization of Autocorrelation Sidelobes and Spectral Interference (JMASSI), to address the dual optimization problem. Our approach involves first converting the dual-objective optimization problem into a single-objective one. Subsequently, we transform the resulting quartic problem into a quadratic form, thereby ensuring the convergence of the cost function.
2) **Convergence Proof**: We provide a rigorous mathematical proof demonstrating the convergence of the JMASSI algorithm. This proof guarantees monotonic convergence to a solution that effectively minimizes autocorrelation sidelobes and spectral stopband levels.
3) **Performance Evaluation**: We assess the performance of the JMASSI algorithm in challenging scenarios and compare its effectiveness with recent algorithms from the literature. Our results demonstrate that JMASSI successfully suppresses waveform energy within interfering frequency bands while maintaining a high-quality ACF.

### C. NOTATION

In the forthcoming sections, we adhere to the following notation conventions: Bold lowercase letters represent vectors, while bold uppercase letters represent matrices. The symbols $|\cdot|$ and $\|\cdot\|$ denote the absolute value and the Euclidean norm, respectively. Furthermore, $(\cdot)^*$, $(\cdot)^T$, and $(\cdot)^H$ signify the complex conjugate, transpose, and Hermitian (conjugate transpose) operations, respectively. The real part and imaginary part are denoted by $\mathrm{Re}\{\cdot\}$ and $\mathrm{Im}\{\cdot\}$, respectively. Additionally, $\mathrm{circshift}(\mathbf{A}, k)$ denotes the $k$-th circular shift of the columns of the matrix $\mathbf{A}$.

## II. OPTIMIZED OBJECTIVE FUNCTION

Let vector $\mathbf{x} = [x_1, x_2, \ldots, x_N]^T \in \mathbb{C}^N$ represent a radar waveform with $N$ samples. The periodic ACF of the radar waveform can be defined as:

$$C_{\mathbf{x}}(r) = \mathbf{x}^H \mathbf{J}_r \mathbf{x}, \tag{1}$$

where $r$ represents the time-lag and $\mathbf{J}_r$ is the circular shift matrix given by:

$$\mathbf{J}_r = \mathrm{circshift}(\mathbf{I}_N, r), \tag{2}$$

and $\mathbf{I}_N$ is the identity matrix. The quality of the waveform ACF is assessed through the measurement of the ISL, which quantifies the overall energy contained in the sidelobes of the ACF as:

$$E_{\mathrm{ISL}} = \sum_{r=1}^{N-1} \left| \mathbf{x}^H \mathbf{J}_r \mathbf{x} \right|^2. \tag{3}$$

For the radar spectral constraint, we assume that the $k$-th licensed radiator operates on a frequency band $B_k = [f_{k_1}, f_{k_2}]$, where $f_{k_1}$ and $f_{k_2}$ are the lower and upper normalized frequencies. The total energy transmitted in the spectral range $B_k$ can be expressed as:

$$\begin{aligned} E_k &= \int_{f_{k_1}}^{f_{k_2}} |X(f)|^2 df \\ &= \sum_{n=0}^{N-1} \sum_{m=0}^{N-1} x_m^* \left[ \int_{f_{k_1}}^{f_{k_2}} e^{j2\pi f(m-n)} df \right] x_n, \end{aligned} \tag{4}$$

where $X(f)$ is the discrete-time Fourier transform (DTFT) of $\mathbf{x}$ given by:

$$X(f) = \sum_{n=0}^{N-1} x(n) e^{-j2\pi fn}.$$

Define an $N \times N$ matrix $\mathbf{G}_k$ whose $(m, n)^{\text{th}}$ element is given by:

$$\mathbf{G}_k(m,n) = \begin{cases} f_{k_2} - f_{k_1}, & \text{if } m = n \\ \dfrac{e^{j2\pi f_{k_2}(m-n)} - e^{j2\pi f_{k_1}(m-n)}}{j2\pi(m-n)}, & \text{otherwise} \end{cases} \tag{5}$$

Then, the total energy $E_k$ in (4) can be expressed as:

$$E_k = \mathbf{x}^H \mathbf{G}_k \mathbf{x}. \tag{6}$$

Thus, the total energy in all stopbands is given by:

$$E_{\text{STOP}} = \sum_{k=1}^{K} \mathbf{x}^H \mathbf{G}_k \mathbf{x}, \tag{7}$$

where $K$ is the total number of the designated stopbands. It is worth mentioning that (6) represents the total energy transmitted within the spectral range $B_k$ and is computed using the DTFT as in (4). This ensures the minimization of the entire spectral energy of the stopband, rather than solely minimizing discrete points within the stopband, which is the case with other approaches that employ the discrete Fourier transform (DFT) for computing stopband spectral energy.

To address the dual objective of minimizing the energy in the sidelobes of the ACF ($E_{\text{ISL}}$ in (3)) and across designated stopbands ($E_{\text{STOP}}$ in (7)), we employ linear weights for both subproblems, merging them into a unified single-objective optimization problem, as follows:

$$f(\mathbf{x}) = (1-\alpha) E_{\text{ISL}} + \alpha E_{\text{STOP}}, \tag{8}$$

where $\alpha \in [0, 1]$ is the weighting factor, which regulates the trade-off between the two subproblems in the optimization process. It is worth mentioning that many studies in the literature incorporated spectral characteristics into the constraints of the optimization problem. However, incorporating the spectral energy into the constraints will force the algorithm to strictly achieve the spectral energy threshold before reducing the ISL, which usually leads to higher ISL. In addition, the spectral energy constraint will be forced in every iteration of the algorithm, leading to increased computational complexity. On the other hand, having fewer constraints increases the problem's feasible area, resulting in a much better solution [22]. Furthermore, the weighted sum of the ISL and stopband spectral energy allows us to prioritize one of them depending on the application.

The optimization problem under the energy constraint (EC) can be formulated as:

$$P = \begin{cases} \min\limits_{\mathbf{x}} & f(\mathbf{x}) \\ \text{s.t.} & \|\mathbf{x}\|_2^2 = 1 \end{cases} \tag{9}$$

Unlike most of the proposed algorithms in the literature that consider the unimodular constraint, we incorporate the energy constraint, which offers more degrees of freedom compared to the unimodular constraint. Since our primary focus is on the quality of the designed waveform, we leverage the energy constraint to exploit these additional degrees of freedom, ultimately enhancing the waveform's quality.

## III. PROPOSED JMASSI ALGORITHM

The objective function in (8) can be expressed as:

$$\begin{aligned} f(\mathbf{x}) &= \bar{\alpha} \sum_{r=1}^{N-1} \left(\mathbf{x}^H \mathbf{J}_r \mathbf{x}\right) \left(\mathbf{x}^H \mathbf{J}_r \mathbf{x}\right)^H + \alpha \sum_{k=1}^{K} \mathbf{x}^H \mathbf{G}_k \mathbf{x} \\ &= \bar{\alpha} \sum_{r=1}^{N-1} \mathbf{x}^H \underbrace{\mathbf{J}_r \mathbf{x}\mathbf{x}^H \mathbf{J}_r^H}_{:=\mathbf{C}_r(\mathbf{x})} \mathbf{x} + \alpha \sum_{k=1}^{K} \mathbf{x}^H \mathbf{G}_k \mathbf{x} \\ &= \bar{\alpha} \sum_{r=1}^{N-1} \mathbf{x}^H \mathbf{C}_r(\mathbf{x}) \mathbf{x} + \alpha \sum_{k=1}^{K} \mathbf{x}^H \mathbf{G}_k \mathbf{x} \\ &= \mathbf{x}^H \mathbf{T}(\mathbf{x}) \mathbf{x}, \end{aligned} \tag{10}$$

where $\bar{\alpha} = 1 - \alpha$, and $\mathbf{T}(\mathbf{x}) = \bar{\alpha} \sum_{r=1}^{N-1} \mathbf{C}_r(\mathbf{x}) + \alpha \sum_{k=1}^{K} \mathbf{G}_k$. Therefore, the optimization problem $P$ in (9) can be re-written as:

$$Q = \begin{cases} \min\limits_{\mathbf{x}} & \mathbf{x}^H \mathbf{T}(\mathbf{x}) \mathbf{x} \\ \text{s.t.} & \|\mathbf{x}\|_2^2 = 1 \end{cases} \tag{11}$$

The problem $Q$ outlined in (11) is a complex-valued problem. To simplify this problem, it is more convenient to transform it into a real-valued one. The real-valued problem of (11) can be given as:

$$\bar{Q} = \begin{cases} \min\limits_{\mathbf{s}} & \mathbf{s}^T \mathbf{R}(\mathbf{x}) \mathbf{s} \\ \text{s.t.} & \mathbf{s}^T \mathbf{s} = 1 \end{cases} \tag{12}$$

where $\mathbf{s}$ and $\mathbf{R}(\mathbf{x})$ are defined as follows:

$$\mathbf{s} = \begin{bmatrix} \text{Re}\{\mathbf{x}\} \\ \text{Im}\{\mathbf{x}\} \end{bmatrix}, \mathbf{R}(\mathbf{x}) = \begin{bmatrix} \text{Re}\{\mathbf{T}(\mathbf{x})\} & -\text{Im}\{\mathbf{T}(\mathbf{x})\} \\ \text{Im}\{\mathbf{T}(\mathbf{x})\} & \text{Re}\{\mathbf{T}(\mathbf{x})\} \end{bmatrix}. \tag{13}$$

The problem $\bar{Q}$ in (12) has been shown to be an NP-hard optimization problem [23]. However, the problem $\bar{Q}$ in (12) can be reduced to a quadratic problem if $\mathbf{x}$ is fixed in $\mathbf{R}(\mathbf{x})$. Therefore, it is possible to formulate an iterative approach to transform the quartic problem into a quadratic one, ensuring the convergence of the cost function. Let $\mathbf{T}_{(n)}$ and $\mathbf{R}_{(n)}$ denote the values of $\mathbf{T}(\mathbf{x})$ and $\mathbf{R}(\mathbf{x})$ at the $n$-th iteration, respectively. The value of $\mathbf{T}_{(n)}$ can be computed as follows:

$$\mathbf{T}_{(n)} = \begin{cases} \bar{\alpha} \sum\limits_{r=1}^{N-1} \mathbf{J}_r \mathbf{x}_{(n)} \mathbf{x}_{(n)}^H \mathbf{J}_r^H + \alpha \sum\limits_{k=1}^{K} \mathbf{G}_k, n = 2k+1 \\ \bar{\alpha} \sum\limits_{r=1}^{N-1} \mathbf{J}_r^H \mathbf{x}_{(n)} \mathbf{x}_{(n)}^H \mathbf{J}_r + \alpha \sum\limits_{k=1}^{K} \mathbf{G}_k^H, n = 2k \end{cases} \tag{14}$$

Then, the iterative version of the problem (12) can be written as:

$$\bar{Q}_{(n)} = \begin{cases} \min\limits_{\mathbf{s}} & \mathbf{s}^T \bar{\mathbf{R}}_{(n-1)} \mathbf{s} \\ \text{s.t.} & \mathbf{s}^T \mathbf{s}_{(n-1)} = 1 \end{cases} \tag{15}$$

where $\bar{\mathbf{R}}_{(n)} = \mathbf{R}_{(n)} + \lambda \mathbf{I}$. The term $\lambda \mathbf{I}$ is added to $\mathbf{R}_{(n)}$ to ensure that $\bar{\mathbf{R}}_{(n)}$ is a positive definite matrix, thereby maintaining the problem $\bar{Q}_{(n)}$ as a strictly convex problem. Including this term does not significantly influence the cost function, provided that $\mathbf{x}$ adheres to the EC. The value of $\lambda$ can be set to any small arbitrary positive number ($\lambda > 0$) [22] that ensures the problem remains strictly convex and that the matrix $\bar{\mathbf{R}}_{(n)}$ is positive definite.

Utilizing the optimality conditions for problem (15), we obtain [22]:

$$\begin{bmatrix} \bar{\mathbf{R}}_{(n-1)} & \mathbf{s}_{(n-1)} \\ \mathbf{s}_{(n-1)}^T & 0 \end{bmatrix} \begin{bmatrix} \mathbf{s}_{(n)} \\ v \end{bmatrix} = \begin{bmatrix} \mathbf{0} \\ 1 \end{bmatrix}, \tag{16}$$

where $v$ is the Lagrangian multiplier of the equality constraints. By applying the Karush-Kuhn-Tucker (KKT) condition [22] and employing block elimination, it can be demonstrated that the stage solution of (15) can be given by:

$$\mathbf{s}_{(n)} = \bar{\mathbf{R}}_{(n-1)}^{-1} \mathbf{s}_{(n-1)} \left( \mathbf{s}_{(n-1)}^T \bar{\mathbf{R}}_{(n-1)}^{-1} \mathbf{s}_{(n-1)} \right)^{-1} \tag{17}$$

and the complex-valued solution $\mathbf{x}_{(n)}$ can be constructed from $\mathbf{s}_{(n)}$ using 13. After certain iterations or when the solution $\mathbf{x}_{(n)}$ meets the EC, the algorithm produces the final solution $\mathbf{x}$.

### A. COMPUTATIONAL COMPLEXITY

The computational complexity of the JMASSI algorithm can be estimated based on the computational cost of solving (16) in each iteration. If the matrix inversion method described in [24] is employed to compute $\mathbf{s}_{(n)}$ in equation (17), the computational complexity per iteration of the JMASSI algorithm can be approximated as $\mathcal{O}(L^{2.373})$, where $L = 2N$ is the length of the vector $\mathbf{s}_{(n)}$.

### B. CONVERGENCE PROOF

The definition of $\mathbf{T}_{(n)}$ in (14) differs depending on whether the iteration index is odd or even. We prove that this selection leads to a monotonically decreasing cost function and guarantees convergence, as described next.

*Lemma 1: Let $\mathbf{s}_{(n)}$ and $\mathbf{s}_{(n-1)}$ be the solutions of $\bar{Q}_{(n)}$ and $\bar{Q}_{(n-1)}$, respectively. Define the function $g(\mathbf{s}_{(n)})$ as*:

$$\begin{aligned} g(\mathbf{s}_{(n)}) &= \mathbf{s}_{(n)}^T \mathbf{R}_{(n)} \mathbf{s}_{(n)} + \lambda \mathbf{s}_{(n)}^T \mathbf{s}_{(n)} \\ &= f(\mathbf{x}_{(n)}) + \lambda \mathbf{x}_{(n)}^H \mathbf{x}_{(n)} \end{aligned}$$

*Then, there exists a finite $\lambda > 0$ such that*:

$$g(\mathbf{s}_{(n-1)}) \geq g(\mathbf{s}_{(n)})$$

*i.e., the sequence $\{g(\mathbf{s}_{(n)})\}_{n=0}^{\infty}$ is non-increasing and converges to a finite value $g^\star$.*

*Proof:* Let $\mathbf{x}_{(n)}$ and $\mathbf{x}_{(n-1)}$ represent the solutions of $Q_{(n)}$ and $Q_{(n-1)}$, respectively. Subsequently, applying the KKT conditions on the *odd* iteration of $\bar{Q}_{(n)}$, yields:

$$2 \sum_{r=1}^{N-1} \mathbf{A}_r \mathbf{s}_{(n-1)} \mathbf{s}_{(n-1)}^T \mathbf{A}_r^T \mathbf{s}_{(n)} + 2\mathbf{B}\mathbf{s}_{(n)} + 2\lambda \mathbf{s}_{(n)} + v\mathbf{s}_{(n-1)} = \mathbf{0} \tag{18a}$$

$$\mathbf{s}_{(n)}^T \mathbf{s}_{(n-1)} = 1, \tag{18b}$$

where

$$\mathbf{A}_r = \sqrt{\bar{\alpha}} \begin{bmatrix} \mathrm{Re}\{\mathbf{J}_r\} & -\mathrm{Im}\{\mathbf{J}_r\} \\ \mathrm{Im}\{\mathbf{J}_r\} & \mathrm{Re}\{\mathbf{J}_r\} \end{bmatrix}, \mathbf{B} = \begin{bmatrix} \mathrm{Re}\{\mathbf{G}\} & -\mathrm{Im}\{\mathbf{G}\} \\ \mathrm{Im}\{\mathbf{G}\} & \mathrm{Re}\{\mathbf{G}\} \end{bmatrix},$$

and $\mathbf{G} = \alpha \sum_{k=1}^{K} \mathbf{G}_k$. The equations in (18) can be rewritten as:

$$2 \sum_{r=1}^{N-1} \mathbf{A}_r \mathbf{y}\mathbf{y}^T \mathbf{A}_r^T \mathbf{z} + 2\mathbf{B}\mathbf{z} + 2\lambda \mathbf{z} + v\mathbf{y} = \mathbf{0} \tag{19a}$$

$$\mathbf{z}^T \mathbf{y} = 1, \tag{19b}$$

where $\mathbf{y} = \mathbf{s}_{(n-1)}$ and $\mathbf{z} = \mathbf{s}_{(n)}$. Define $\mathbf{d} = \mathbf{y}/\beta - \mathbf{z}$ where $\beta = \mathbf{y}^T\mathbf{y}$ and $\mathbf{d} \neq \mathbf{0}$. Since $\mathbf{s}_{(n)}^T \mathbf{s}_{(n-1)} = \mathbf{z}^T\mathbf{y} = 1$, then $\mathbf{d}^T\mathbf{y} = 0$. Therefore, multiplying (19a) by $\mathbf{d}^T$ yields:

$$\sum_{r=1}^{N-1} \mathbf{d}^T \mathbf{A}_r \mathbf{y}\mathbf{y}^T \mathbf{A}_r^T \mathbf{z} + \mathbf{d}^T \mathbf{B}\mathbf{z} + \lambda \mathbf{d}^T \mathbf{z} = 0. \tag{20}$$

Taking the transpose of (20) and noting that $\mathbf{B} = \mathbf{B}^T$, we obtain:

$$\sum_{r=1}^{N-1} \mathbf{z}^T \mathbf{A}_r \mathbf{y}\mathbf{y}^T \mathbf{A}_r^T \mathbf{d} + \mathbf{z}^T \mathbf{B}\mathbf{d} + \lambda \mathbf{z}^T \mathbf{d} = 0. \tag{21}$$

Without loss of generality, let $\beta = 1$, then $\mathbf{y} = \mathbf{z} + \mathbf{d}$. Thus, we have:

$$g(\mathbf{s}_{(n-1)}) = \sum_{r=1}^{N-1} \mathbf{y}^T \mathbf{A}_r \mathbf{y}\mathbf{y}^T \mathbf{A}_r^T \mathbf{y} + \mathbf{y}^T \mathbf{B}\mathbf{y} + \lambda \mathbf{y}^T \mathbf{y}. \tag{22}$$

By substituting $\mathbf{y} = \mathbf{z} + \mathbf{d}$ in (22), we get:

$$\begin{aligned} g(\mathbf{s}_{(n-1)}) = &\sum_{r=1}^{N-1} (\mathbf{z}+\mathbf{d})^T \mathbf{A}_r \mathbf{y}\mathbf{y}^T \mathbf{A}_r^T (\mathbf{z}+\mathbf{d}) \\ &+ (\mathbf{z}+\mathbf{d})^T \mathbf{B}(\mathbf{z}+\mathbf{d}) + \lambda (\mathbf{z}+\mathbf{d})^T (\mathbf{z}+\mathbf{d}). \end{aligned} \tag{23}$$

Expanding (23) and subsequently rearranging the resulting terms yields:

$$\begin{aligned} g(\mathbf{s}_{(n-1)}) = &\underbrace{\sum_{r=1}^{N-1} \mathbf{z}^T \mathbf{A}_r \mathbf{y}\mathbf{y}^T \mathbf{A}_r^T \mathbf{z} + \mathbf{z}^T \mathbf{B}\mathbf{z} + \lambda \mathbf{z}^T \mathbf{z}}_{:= g_e(\mathbf{s}_{(n)}) \text{ (corresponds to the } even \text{ iteration)}} \\ &+ \underbrace{\sum_{r=1}^{N-1} \mathbf{d}^T \mathbf{A}_r \mathbf{y}\mathbf{y}^T \mathbf{A}_r^T \mathbf{z} + \mathbf{d}^T \mathbf{B}\mathbf{z} + \lambda \mathbf{d}^T \mathbf{z}}_{= 0 \text{ (from (20))}} \\ &+ \underbrace{\sum_{r=1}^{N-1} \mathbf{z}^T \mathbf{A}_r \mathbf{y}\mathbf{y}^T \mathbf{A}_r^T \mathbf{d} + \mathbf{z}^T \mathbf{B}\mathbf{d} + \lambda \mathbf{z}^T \mathbf{d}}_{= 0 \text{ (from (21))}} \end{aligned}$$

$$+\underbrace{\sum_{r=1}^{N-1}\mathbf{d}^T\mathbf{A}_r\mathbf{y}\mathbf{y}^T\mathbf{A}_r^T\mathbf{d}+\mathbf{d}^T\mathbf{B}\mathbf{d}+\lambda\mathbf{d}^T\mathbf{d}}_{:=h(\mathbf{d},\mathbf{y})}. \quad (24)$$

Therefore,

$$g(\mathbf{s}_{(n-1)})=g_e(\mathbf{s}_{(n)})+h(\mathbf{d},\mathbf{y}). \quad (25)$$

For the even iteration, we have

$$g_e(\mathbf{s}_{(n)})=\sum_{r=1}^{N-1}\left(\mathbf{z}^T\mathbf{A}_r\mathbf{y}\right)\left(\mathbf{y}^T\mathbf{A}_r^T\mathbf{z}\right)+\mathbf{z}^T\mathbf{B}\mathbf{z}+\lambda\mathbf{z}^T\mathbf{z}. \quad (26)$$

By rearranging (26), we obtain:

$$g_e(\mathbf{s}_{(n)})=\sum_{r=1}^{N-1}\left(\mathbf{y}^T\mathbf{A}_r^T\mathbf{z}\right)\left(\mathbf{z}^T\mathbf{A}_r\mathbf{y}\right)+\mathbf{z}^T\mathbf{B}\mathbf{z}+\lambda\mathbf{z}^T\mathbf{z}. \quad (27)$$

By substituting (27) in (25) and noting that $\mathbf{y}=\mathbf{z}+\mathbf{d}$, we obtain:

$$\begin{aligned}g(\mathbf{s}_{(n-1)})=&\underbrace{\sum_{r=1}^{N-1}\mathbf{z}^T\mathbf{A}_r^T\mathbf{z}\mathbf{z}^T\mathbf{A}_r\mathbf{z}+\mathbf{z}^T\mathbf{B}\mathbf{z}+\lambda\mathbf{z}^T\mathbf{z}}_{g(\mathbf{s}_{(n)})}\\&+\underbrace{\mathbf{d}^T\left(\sum_{r=1}^{N-1}\mathbf{A}_r\mathbf{y}\mathbf{y}^T\mathbf{A}_r^T+\sum_{r=1}^{N-1}\mathbf{A}_r^T\mathbf{z}\mathbf{z}^T\mathbf{A}_r\right)\mathbf{d}}_{\geq 0}\\&+\underbrace{\mathbf{d}^T\mathbf{B}\mathbf{d}+\lambda\mathbf{d}^T\mathbf{d}}_{\geq 0}+\mathbf{d}^T\mathbf{W}\mathbf{z}+\mathbf{z}^T\mathbf{W}\mathbf{d}, \quad (28)\end{aligned}$$

where $\mathbf{W}=\sum_{r=1}^{N-1}\mathbf{A}_r^T\mathbf{z}\mathbf{z}^T\mathbf{A}_r$. If we set

$$\lambda\geq\frac{-\mathbf{d}^T\mathbf{W}\mathbf{z}-\mathbf{z}^T\mathbf{W}\mathbf{d}}{\mathbf{d}^T\mathbf{d}},$$

then $\lambda\mathbf{d}^T\mathbf{d}+\mathbf{d}^T\mathbf{W}\mathbf{z}+\mathbf{z}^T\mathbf{W}\mathbf{d}\geq 0$. Since $\mathbf{d}^T\mathbf{d}>0$ and $\|\mathbf{z}\|$ is bounded, then:

$$\frac{-\mathbf{d}^T\mathbf{W}\mathbf{z}-\mathbf{z}^T\mathbf{W}\mathbf{d}}{\mathbf{d}^T\mathbf{d}}$$

is also bounded and $\lambda$ is a finite value. Therefore,

$$g(\mathbf{s}_{(n-1)})\geq g(\mathbf{s}_{(n)}).$$

Since $g(\mathbf{s}_{(n)})\geq 0$ for all $n$ then $g(\mathbf{s}_{(n)})$ is bounded and converges to a finite value $g^\star$. □

The procedural details of waveform design utilizing the JMASSI Algorithm are described in Algorithm 1.

**Algorithm 1** JMASSI

Initial setup of $N, f_{k_1}, f_{k_2}, \alpha, \lambda, \epsilon$
Randomly initialize $\mathbf{x}_{(0)}$
Compute $\mathbf{G}_k,\ \forall k\in\{1,\cdots,K\}$
**for** $r$ in $\{(1,N-1)\}$ **do**
    Compute $\mathbf{J}_r$ as in (2)
**end for**
$n\leftarrow 1$
**repeat**
    **if** $n$ is odd **then**
        $\mathbf{T}_{(n)}\leftarrow\bar{\alpha}\sum_{r=1}^{N-1}\mathbf{J}_r\mathbf{x}_{(n-1)}\mathbf{x}_{(n-1)}^H\mathbf{J}_r^H+\alpha\sum_{k=1}^{K}\mathbf{G}_k$
    **else**
        $\mathbf{T}_{(n)}\leftarrow\bar{\alpha}\sum_{r=1}^{N-1}\mathbf{J}_r^H\mathbf{x}_{(n-1)}\mathbf{x}_{(n-1)}^H\mathbf{J}_r+\alpha\sum_{k=1}^{K}\mathbf{G}_k^H$
    **end if**
    Compute $\mathbf{s}_{(n-1)}$ and $\bar{\mathbf{R}}_{(n-1)}$
    $\mathbf{s}_{(n)}=\bar{\mathbf{R}}_{(n-1)}^{-1}\mathbf{s}_{(n-1)}\left(\mathbf{s}_{(n-1)}^T\bar{\mathbf{R}}_{(n-1)}^{-1}\mathbf{s}_{(n-1)}\right)^{-1}$
    Compute $\mathbf{x}_{(n)}$ from $\mathbf{s}_{(n)}$
    $n\leftarrow n+1$
**until** $\|\mathbf{x}_{(n)}-\mathbf{x}_{(n-1)}\|\leq\epsilon$
$\mathbf{x}\leftarrow\mathbf{x}_{(n)}$

## IV. NUMERICAL RESULTS

In this section, we employ computer simulations to demonstrate the potential of JMASSI algorithm in various scenarios. The performance is compared with two recent algorithms, namely, AM-EPA [19] and LBSD [21]. Our primary focus is evaluating the quality of the designed waveform based on two performance metrics: the level of autocorrelation sidelobes and the level of stopbands in the waveform spectrum. It is important to note that the presence of stopbands in the waveform spectrum can potentially result in increased autocorrelation sidelobes, thereby affecting the quality of the designed waveform. This degradation becomes more pronounced as the size and the number of the stopbands increase. Hence, we assess the effectiveness of our proposed algorithm in reducing the autocorrelation sidelobes and the stopband levels and balancing these conflicting objectives in different scenarios. We conducted three scenarios to evaluate the proposed algorithm performance under varying degrees of complexity. In the first scenario, we evaluate the algorithm in designing waveforms with a single stopband occupying 25% of the total band. This scenario served as a baseline to gauge the algorithm's performance under relatively simpler conditions. Subsequently, we increased the challenge in the second scenario by designing waveforms with a single stopband occupying 50% of the total bandwidth. Finally, in the third scenario, we further increased the challenge by designing waveforms with three stopbands that collectively occupied 50% of the total bandwidth. This scenario aimed to evaluate the algorithm's effectiveness in managing multiple stopbands simultaneously.

Waveforms consisting of $N=256$ samples are generated. All algorithms start with the same random sequence. We set $\lambda=10^{-5}$ for JMASSI and $\alpha=0.9$ for both LBSD and JMASSI. To ensure consistency, we establish a unified stopping criterion for LBSD and JMASSI algorithms, halting the simulation when the Euclidean distance between the designed waveforms in two successive iterations falls below a specified threshold $\epsilon=10^{-4}$. For AM-EPA, we set $w=0.9$, $U_{\max}=0.8095$, $\epsilon_x=10^{-3}$, $\epsilon_{\text{rank}}=10^{-8}$, $\phi_{\max}=50$. For more details about these parameters, the reader is referred to [19]. The results are presented against the normalized frequency $f/f_s$ computed at 320 spectral points, where $f_s$ is the sampling frequency.

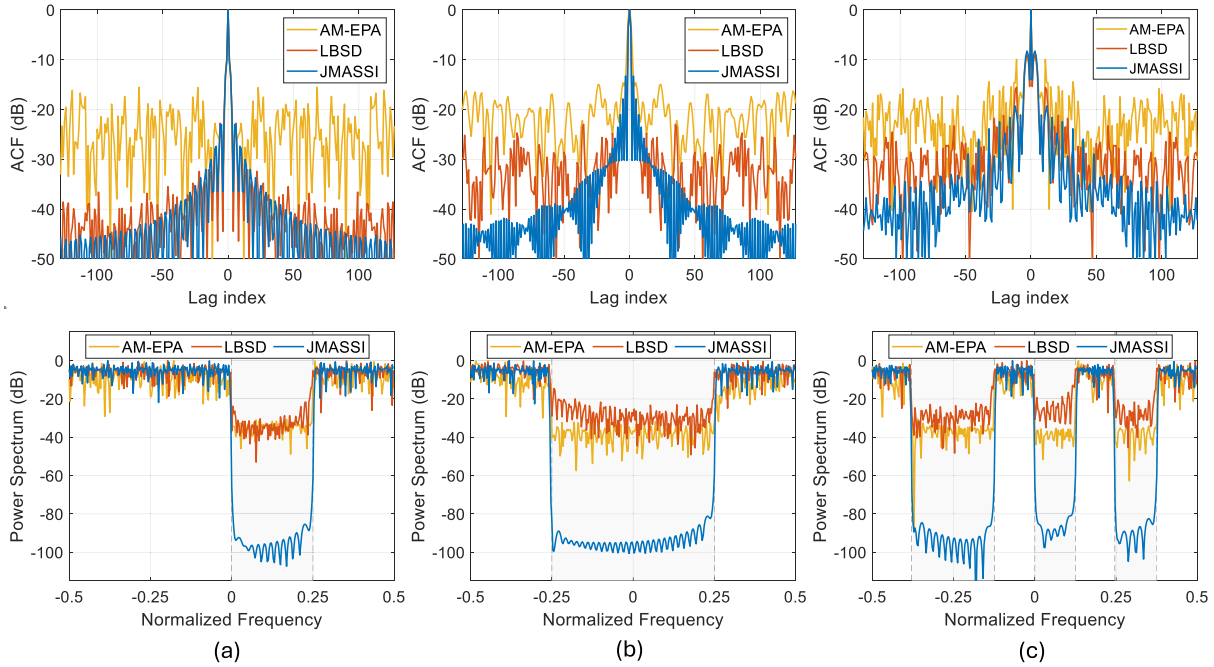


**FIGURE 1.** ACFs and power spectra of AM-EPA, LBSD, and JMASSI algorithms. (a) Scenario 1. (b) Scenario 2. (c) Scenario 3.

Fig. 1 depicts the ACFs (top row) and power spectra (second row) generated by AM-EPA, LBSD, and JMASSI algorithms in the three scenarios. Fig. 1(a) depicts the results of the first scenario, where we consider a single stopband occupying 25% of the total band. The start and end normalized frequencies of the stopband are 0 and 0.25, respectively (i.e. the normalized interval of the stopband is $[0, 0.25]$). As can be observed, the AM-EPA algorithm exhibits the least favorable autocorrelation performance with a sidelobe level of about $-16$ dB relative to the peak value. Conversely, the LBSD algorithm demonstrates improved autocorrelation, with some fluctuating sidelobes. In contrast, the proposed JMASSI algorithm outperforms AM-EPA and LBSD, showcasing superior autocorrelation with decaying sidelobes. From the power spectra of these waveforms, we can observe that the stopband levels of AM-EPA and LBSD are about $-30$ dB and $-20$ dB, respectively. In contrast, the proposed JMASSI exhibits a significantly lower stopband level, surpassing the others with a remarkable performance of less than $-80$ dB. This clear superiority in stopband level highlights the exceptional quality and effectiveness of the JMASSI method compared to alternative approaches.

Fig. 1(b) depicts the results of the second scenario, where we consider a single stopband occupying 50% of the total band. The normalized interval of the stopband is $[-0.25, 0.25]$. In addition, Fig. 1(c) depicts the results of the third scenario, where we consider three stopbands occupying 25%, 12.5%, and 12.5% of the total band. The normalized intervals of the first, second, and third stopbands are $[-0.375, -0.125]$, $[0, 0.125]$, and $[0.25, 0.375]$, respectively. Similar observations can be drawn from these figures,

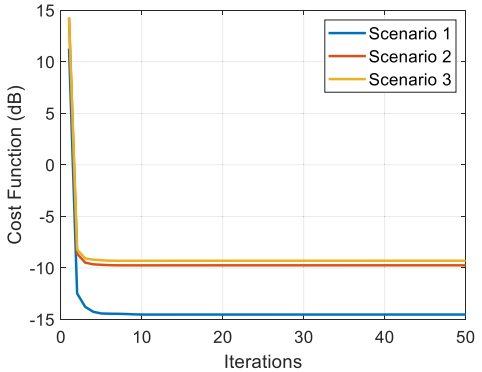


**FIGURE 2.** Convergence of the proposed JMASSI algorithm.

where the proposed JMASSI algorithm outperforms both AM-EPA and LBSD in terms of the autocorrelation sidelobes level and the stopband level.

Fig. 2 shows that the cost function of the proposed JMASSI algorithm is monotonically decreasing for all three scenarios and that it converges after approximately 5 iterations.

To assess the convergence speed of the proposed JMASSI algorithm compared to other algorithms, we performed waveform design experiments in three different scenarios. These experiments were conducted on a computer with an Intel i7-8750H 2.20GHz CPU and 16 GB RAM using the MATLAB® R2022a environment. We carried out 1000 trials with independent random initial sequences of length $N = 128$ for each scenario, setting the stopping criteria to $10^{-3}$. Due to the low speed of the AM-EPA method, we limited our trials for this method to 10. The comparison metrics included the number of iterations for convergence, the convergence time, and the optimal value of the cost function. Table 1

**TABLE 1. Convergence speed and optimal value of the objective function.**

| Method | Scenario 1 | | | Scenario 2 | | | Scenario 3 | | |
|---|---|---|---|---|---|---|---|---|---|
| | #iterations | Time (s) | Optimal cost (dB) | #iterations | Time (s) | Optimal cost (dB) | #iterations | Time (s) | Optimal cost (dB) |
| AM-EPA | 119 | 1221 | -7.32 | 236 | 2767 | -4.75 | 1445 | 6893 | -4.71 |
| LBSD | 1741 | 0.128 | -11.4 | 1894 | 0.149 | -5.73 | 1487 | 0.12 | -5.86 |
| JMASSI | 168 | 1.973 | -14.37 | 235 | 2.745 | -9.57 | 507 | 6.89 | -8.88 |

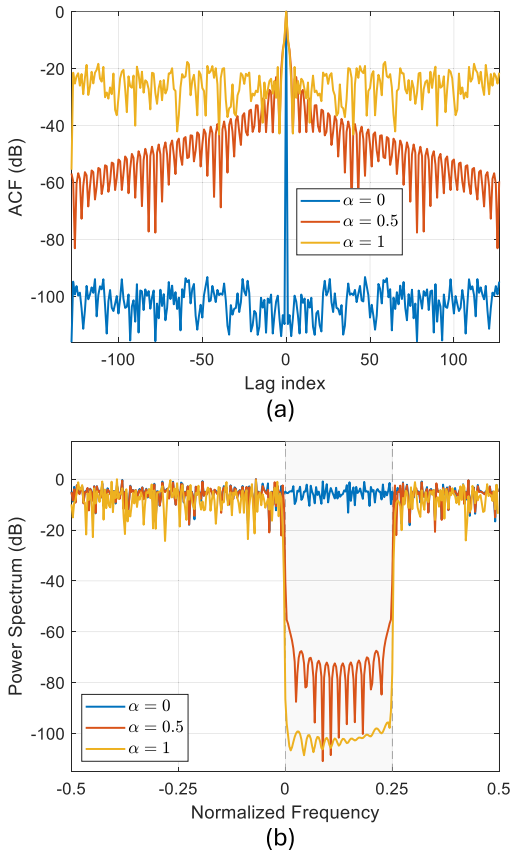


**FIGURE 3. Performance of JMASSI under different weighting factor $\alpha$ values. (a) ACFs. (b) Power spectra.**

summarizes the results averaged over the number of trials. In terms of convergence time, the AM-EPA method was the slowest, with convergence times extending to tens of minutes in all scenarios. The LBSD method exhibited the fastest convergence across all scenarios, with convergence times measured in fractions of a second. The JMASSI method demonstrated convergence times measured in a few seconds. Regarding the optimal value of the objective function, the proposed JMASSI method consistently achieved the lowest average optimal value compared to the other methods across all scenarios. Although the proposed method is not as fast as the LBSD method, it provides superior performance in terms of the optimal value of the cost function with reasonable convergence times.

To demonstrate the performance of the proposed JMASSI algorithm across different weighting factors $\alpha$, we designed waveforms with a single stopband, similar to the first scenario, and varied the values of $\alpha$. Fig. 3 shows the results for $\alpha$ values of 0, 0.5, and 1. Fig. 3(a) presents the ACFs of the designed waveforms, while Fig. 3(b) illustrates their spectra. When $\alpha = 0$, indicating a complete emphasis on minimizing the ISL, the ACF of the designed waveform exhibits an impulse-like shape with sidelobe level minimized to approximately $-100$ dB. Correspondingly, the waveform spectrum shows no presence of a stopband, as expected. When $\alpha = 0.5$, the autocorrelation sidelobes increased. For instance, at lag cell 50, the sidelobe level measures approximately $-40$ dB. Correspondingly, the spectrum of the designed waveform exhibits a stopband with a level below $-60$ dB. Lastly, when $\alpha = 1$, indicating a complete emphasis on minimizing the stopband level, the autocorrelation sidelobes significantly increased. For instance, at lag cell 50, the sidelobe level measures approximately $-20$ dB. In this case, the spectrum of the designed waveform exhibits a stopband with a level of approximately $-100$ dB. From Fig. 3, we can observe the effectiveness of the proposed JMASSI algorithm in balancing these conflicting objectives, i.e., minimizing the autocorrelation sidelobes and the stopband level. The weighting factor $\alpha$ enables prioritizing one of these objectives depending on the specific application requirements.

## V. CONCLUSION

In this paper, a novel algorithm that addresses the dual optimization of ACF and spectral characteristics of radar waveform is developed. The proposed JMASSI algorithm enables the generation of radar waveforms characterized by minimal stopband levels and autocorrelation sidelobe levels. The proposed JMASSI algorithm can generate waveforms with multiple stopbands with a suppression gain of approximately 50 dB over some recently proposed algorithms while preserving superior ACF. The convergence of JMASSI is rigorously demonstrated through mathematical proof, providing a robust basis for practical application.

## REFERENCES

[1] H. He, J. Li, and P. Stoica, *Waveform Design for Active Sensing Systems: A Computational Approach*. Cambridge, U.K.: Cambridge Univ. Press, 2012.

[2] Y. Li and S. A. Vorobyov, "Fast algorithms for designing unimodular Waveform(s) with good correlation properties," *IEEE Trans. Signal Process.*, vol. 66, no. 5, pp. 1197–1212, Mar. 2018.

[3] Z. Lin, W. Pu, and Z.-Q. Luo, "Minimax design of constant modulus MIMO waveforms for active sensing," *IEEE Signal Process. Lett.*, vol. 26, no. 10, pp. 1531–1535, Oct. 2019.

[4] M. Xia, S. Chen, and X. Yang, "Novel method for designing waveform with good correlation properties based on high-order norm unified representation," *IEEE Access*, vol. 10, pp. 108440–108452, 2022.

[5] K. Zhong, J. Hu, and C. Pan, "Constant modulus MIMO radar waveform design via iterative optimization network method," *IEEE Trans. Instrum. Meas.*, vol. 72, pp. 1–11, 2023.

[6] E. M. Almohimmah, A. M. Ragheb, A. Almaiman, O. S. Aldayel, and S. A. Alshebeili, "Enabling block-sparse recovery in photonics-based radars with multi-waveform transmission," *J. Lightw. Technol.*, vol. 42, no. 7, pp. 2303–2316, Apr. 15, 2024.

[7] N. Neuberger and R. Vehmas, "A costas-based waveform for local range-Doppler sidelobe level reduction," *IEEE Signal Process. Lett.*, vol. 28, pp. 673–677, 2021.
[8] E. M. Almohimmah, O. Aldayel, J. Ali, A. M. Ragheb, A. Almaiman, M. A. Esmail, and S. A. Alshebeili, "Performance investigation of an ambiguity function-shaped waveform (AFSW) using a photonics-based radar system," *Opt. Exp.*, vol. 31, no. 3, pp. 3784–3803, Jan. 2023.
[9] Z. Cheng, Z. He, S. Zhang, and J. Li, "Constant modulus waveform design for MIMO radar transmit beampattern," *IEEE Trans. Signal Process.*, vol. 65, no. 18, pp. 4912–4923, Sep. 2017.
[10] J. Yang, G. Cui, X. Yu, and L. Kong, "Quartic optimization for MIMO radar transmit beampattern synthesis," in *Proc. IEEE Int. Conf. Signal, Inf. Data Process. (ICSIDP)*, Dec. 2019, pp. 1–5.
[11] L. Lan, M. Rosamilia, A. Aubry, A. De Maio, and G. Liao, "FDA-MIMO transmitter and receiver optimization," *IEEE Trans. Signal Process.*, vol. 72, pp. 1576–1589, 2024.
[12] L. Lan, A. Marino, A. Aubry, A. De Maio, G. Liao, J. Xu, and Y. Zhang, "GLRT-based adaptive target detection in FDA-MIMO radar," *IEEE Trans. Aerosp. Electron. Syst.*, vol. 57, no. 1, pp. 597–613, Feb. 2021.
[13] W. Rowe, P. Stoica, and J. Li, "Spectrally constrained waveform design [sp Tips&Tricks]," *IEEE Signal Process. Mag.*, vol. 31, no. 3, pp. 157–162, May 2014.
[14] X. Zhang and X. Wang, "Waveform design with controllable modulus dynamic range under spectral constraints," *Signal Process.*, vol. 189, Dec. 2021, Art. no. 108285.
[15] B. Tang, J. Liu, H. Wang, and Y. Hu, "Constrained radar waveform design for range profiling," *IEEE Trans. Signal Process.*, vol. 69, pp. 1924–1937, 2021.
[16] H. He, P. Stoica, and J. Li, "Waveform design with stopband and correlation constraints for cognitive radar," in *Proc. 2nd Int. Workshop Cogn. Inf. Process.*, Jun. 2010, pp. 344–349.
[17] J. Liang, H. C. So, C. S. Leung, J. Li, and A. Farina, "Waveform design with unit modulus and spectral shape constraints via Lagrange programming neural network," *IEEE J. Sel. Topics Signal Process.*, vol. 9, no. 8, pp. 1377–1386, Dec. 2015.
[18] L. Tang, Y. Zhu, and Q. Fu, "Fast algorithm for designing periodic/aperiodic sequences with good correlation and stopband properties," *EURASIP J. Adv. Signal Process.*, vol. 2018, no. 1, p. 57, Dec. 2018.
[19] C.-W. Huang, L.-F. Chen, and B. Su, "Waveform design for optimal PSL under spectral and unimodular constraints via alternating minimization," *IEEE Trans. Signal Process.*, vol. 71, pp. 2518–2531, 2023.
[20] CVX Research. (Jan. 2020). *CVX: MATLAB Software for Disciplined Convex Programming, Version 2.2*. [Online]. Available: http://cvxr.com/cvx
[21] K. Savci, "A limited memory BFGS based unimodular sequence design algorithm for spectrum-aware sensing systems," *IEEE Access*, vol. 10, pp. 77011–77029, 2022.
[22] S. P. Boyd and L. Vandenberghe, *Convex Optimization*. Cambridge, U.K.: Cambridge Univ. Press, 2004.
[23] A. Aubry, A. De Maio, B. Jiang, and S. Zhang, "Ambiguity function shaping for cognitive radar via complex quartic optimization," *IEEE Trans. Signal Process.*, vol. 61, no. 22, pp. 5603–5619, Nov. 2013.
[24] V. V. Williams, "Multiplying matrices faster than coppersmith-winograd," in *Proc. 44th Annu. ACM Symp. Theory Comput.*, May 2012, pp. 887–898.

**OMAR ALDAYEL** (Member, IEEE) received the B.S. degree from King Saud University, Riyadh, Saudi Arabia, in 2007, the M.S. degree from the KTH Royal Institute of Technology, Stockholm, Sweden, in 2011, and the Ph.D. degree in electrical engineering from The Pennsylvania State University, University Park, PA, USA, in 2017. He was with King Saud University, as a Lecturer, from 2011 to 2013, where he is currently an Assistant Professor with the Department of Electrical Engineering. His research interests include statistical signal processing and optimization theory with its application to radar signal processing and wireless communications.

**ESAM M. ALMOHIMMAH** received the bachelor's degree (Hons.) in electrical engineering from Sana'a University, Yemen, and the M.Sc. degree in electrical engineering from King Saud University, Riyadh, Saudi Arabia, where he is currently pursuing the Ph.D. degree with the Department of Electrical Engineering. His research interests include optical and wireless communications, radars, photonics-based radars, and advanced radar signal processing.

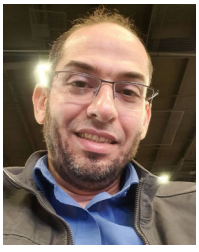

**AMR M. RAGHEB** was a full-time Researcher with the Prince Sultan Advanced Technology Research Institute (PSATRI), Riyadh, Saudi Arabia, in 2012, and the Digital Photonic Test Division, Keysight Technologies, Boeblingen, Germany, in 2013. He has over ten years of experience with the Photonics Telecommunication Laboratory. He is currently an Associate Professor with the Electrical Engineering Department, King Saud University, where he is also the Director of the Photonics Laboratory, Technology Innovation Center in RF and Photonics (RFTONICS), College of Engineering. His research interests include photonic-microwave integration, quantum dash-based lasers, free-space optical communication, optical modulation format identification, coherent optical receivers, multi-format highspeed optical transmitter, and passive optical networks.

**AHMED ALMAIMAN** received the bachelor's degree in electrical engineering from King Saud University, Saudi Arabia, and the M.S. and Ph.D. degrees from the University of Southern California (USC), Los Angeles, CA, USA, in 2014 and 2018, respectively. He is currently a Faculty Member with King Saud University.

**SALEH A. ALSHEBEILI** was the Chairperson of the Electrical Engineering Department, King Saud University, Riyadh, Saudi Arabia, from 2001 to 2005. He has more than 30 years of teaching and research experience in the area of communications and signal processing. He was a member of the Board of Director with the King Abdullah Institute for Research and Consulting Studies, from 2007 to 2009, and a member with the Prince Sultan Advanced Technologies Research Institute, from 2008 to 2017, where he was the Managing Director, from 2008 to 2011, and the Director of the Saudi-Telecom Research Chair, from 2008 to 2012. He has been the Director of the Technology Innovation Center, RF and Photonics in e-Society, funded by King Abdulaziz City for Science and Technology (KACST), since 2011. He is currently a Professor with the Electrical Engineering Department, King Saud University, and a member with the Spectrum Advisory Group formed by the Communications, Space, and Technology Commission, Saudi Arabia.